



Deposited via The University of Leeds.

White Rose Research Online URL for this paper:

<https://eprints.whiterose.ac.uk/id/eprint/186066/>

Version: Accepted Version

Article:

Gómez, GC, Walsh, C and Palau, A (2022) Different molecular filament widths as tracers of accretion onto filaments. *Monthly Notices of the Royal Astronomical Society*. ISSN: 0035-8711

<https://doi.org/10.1093/mnras/stac912>

© 2022 The Author(s) Published by Oxford University Press on behalf of the Royal Astronomical Society. This is an author produced version of an article published in *Monthly Notices of the Royal Astronomical Society*. Uploaded in accordance with the publisher's self-archiving policy.

Reuse

Items deposited in White Rose Research Online are protected by copyright, with all rights reserved unless indicated otherwise. They may be downloaded and/or printed for private study, or other acts as permitted by national copyright laws. The publisher or other rights holders may allow further reproduction and re-use of the full text version. This is indicated by the licence information on the White Rose Research Online record for the item.

Takedown

If you consider content in White Rose Research Online to be in breach of UK law, please notify us by emailing eprints@whiterose.ac.uk including the URL of the record and the reason for the withdrawal request.

Different molecular filament widths as tracers of accretion onto filaments

Gilberto C. Gómez,^{1*} Catherine Walsh,² and Aina Palau¹

¹*Instituto de Radioastronomía y Astrofísica, Universidad Nacional Autónoma de México, Antigua Carretera a Pátzcuaro # 8701, Ex-Hda. San José de la Huerta, Morelia, Michoacán, México C.P. 58089*

²*School of Physics and Astronomy, University of Leeds, Leeds, UK LS2 9JT*

Accepted XXX. Received YYY; in original form ZZZ

ABSTRACT

We explore how dense filament widths, when measured using different molecular species, may change as a consequence of gas accretion toward the filament. As a gas parcel falls into the filament, it will experience different density, temperature, and extinction values. The rate at which this environment changes will affect differently the abundance of different molecules. So, a molecule that forms quickly will better reflect the local physical conditions a gas parcel experiences than a slower-forming molecule. Since these differences depend on how the respective timescales compare, the different molecular distributions should reflect how rapidly the environment changes, i.e., the accretion rate toward the filament. We find that the filament widths measured from time-dependent abundances for C₂H, CO, CN, CS, and C₃H₂, are the most sensitive to this effect. This is because these molecules are the ones presenting also the wider filament widths. On the contrary, molecules such as N₂H⁺, NH₃, H₂CO, HNC and CH₃OH are not so sensitive to accretion and present the narrowest filament widths. We propose that ratios of filament widths for different tracers could be a useful tool to estimate the accretion rate onto the filament.

Key words: ISM: clouds – ISM: kinematics and dynamics – ISM: molecules – astrochemistry

1 INTRODUCTION

The filamentary nature of molecular clouds has been clearly demonstrated in the astronomical literature, specially through observations of the thermal emission from dust (André et al. 2014; Molinari et al. 2010; Wang et al. 2015; Hacar et al. 2018; Planck Collaboration et al. 2016, among others). The filaments embedded in the clouds are frequently organized in hub-filament systems. Longitudinal gas flow directs material to the hubs sitting at the intersection of two or more filaments and, while it has been suggested that these hubs are the sites of high-mass star formation, it is a matter of debate (Peretto et al. 2013; Henshaw et al. 2014; Yuan et al. 2018; Lu et al. 2018; Dewangan et al. 2020). At the same time, molecular filaments are observed to contain cores, usually as result of gravitational fragmentation within the filament. Star formation within these embedded cores constitutes a non-trivial source of low- and intermediate-mass stars (André et al. 2014; Tafalla & Hacar 2015). Although the internal density and velocity structure of molecular filaments would help us understand the mass

reservoir available for star formation, the details of this mass flow and its impact on the star formation phenomenon is still an open question in the community. Different models have been proposed for their internal structure, but observations that discern between those models are elusive.

The simplest models assume that molecular filaments are structures in hydrostatic equilibrium (Stodólkiewicz 1963; Ostriker 1964; Inutsuka & Miyama 1992; Fischera & Martin 2012; Burge et al. 2016). However, these do not include a mechanism for the origin for the filamentary structure. In contrast, another set of models state that the filaments are formed where turbulent flows within the cloud meet (e.g. Padoan et al. 2001; Auddy et al. 2016), although this convergence of flows may not be a consequence of turbulence but of the global gravitational collapse of the cloud (Heitsch 2013a,b; Hennebelle & André 2013; Zamora-Avilés et al. 2017).

In a spherically-symmetric collapse, the mass that flows across a constant-radius surface has to be conserved, and so this flux equates to the time derivative of the mass within the given surface. In contrast, in the case of a collapsing filament, the rate of change of mass within a given cylindrical radius does not have to be equal to the mass flux across

* E-mail: g.gomez@irya.unam.mx

that radius since the mass may be evacuated in the longitudinal direction, in a similar fashion to a squeezed toothpaste tube. So, a filament formed due to the global collapse of a cloud acts as a funnel that redirects the gas around the cloud towards star-forming clumps located at the hubs where filaments meet, or to the smaller mass clumps formed within the filaments themselves. In this picture, proposed by [Gómez & Vázquez-Semadeni \(2014, GV14 from here on\)](#), the molecular filaments are not material but river-like flow structures along which the gas falls down the large-scale gravitational well. Note that this model relies on gravitational collapse only and does not require external agents to direct the gas to flow along the filaments (for example, [Balsara et al. 2001](#)).

Longitudinal flows consistent with the scenario described above have been widely observed in a number of filamentary molecular clouds such as Taurus ([Dobashi et al. 2019](#)), Serpens ([Kirk et al. 2013](#); [Lee et al. 2014](#); [Fernández-López et al. 2014](#); [Gong et al. 2018](#)), Musca ([Bonne et al. 2020](#)), DR21 ([Hu et al. 2021](#)), clouds of the Galactic Center (SgrB2(N), [Schwörer et al. 2019](#)), or filamentary high-mass star-forming regions (e.g., [Peretto et al. 2014](#); [Tackenberg et al. 2014](#); [Lu et al. 2018](#); [Veena et al. 2018](#); [Yuan et al. 2018](#); [Chen et al. 2019](#); [Issac et al. 2019](#); [Treviño-Morales et al. 2019](#); [Chung et al. 2021](#); [Liu et al. 2021](#); [Ren et al. 2021](#)). In addition, possible signs of accretion onto filaments have also been reported in the literature (e.g., [Gong et al. 2018](#); [Shimajiri et al. 2019](#); [Chen et al. 2020b,a](#); [Sepúlveda et al. 2020](#); [Zhang et al. 2020](#); [Gong et al. 2021](#)). Furthermore, magnetic structures derived from the longitudinal flow might be used to determine the physical conditions of the gas ([Gómez et al. 2018](#)). A few recent works have reported the detection of a change in the magnetic field orientation from perpendicular to the filament outside the filament to parallel inside it ([Qiu et al. 2013](#); [Pillai et al. 2020](#); [Arzoumanian et al. 2021](#); [Palau et al. 2021](#)). All these observed properties (velocity gradients along the filaments, accretion onto the filaments, and change in the magnetic field orientation from perpendicular to parallel to the filament) are consistent with the results of the simulations of GV14 and [Gómez et al. \(2018\)](#).

The ‘filaments as flow structures’ model naturally arises from the global hierarchical collapse model (GHC, [Vázquez-Semadeni et al. 2019](#)), in which the clouds are pictured as containing collapsing regions within larger-scale collapses, each scale accreting from larger ones. As the warm neutral medium experiences a compression and undergoes a phase transition to cold neutral medium ([Hennebelle & Pérault 1999](#); [Koyama & Inutsuka 2002](#)), its density increases by a factor of ~ 100 , while its temperature decreases by a similar factor. As a consequence, the Jeans mass in the recently formed cloud drops by a factor of $\sim 10^4$, and so the collapse proceeds in an almost pressureless fashion. Filaments formed in this scenario arise from the anisotropic collapse of the gravitationally unstable structure, in which a triaxial spheroid collapses along its shortest dimension first, thus sequentially forming sheets and filaments ([Lin et al. 1965](#)). In this sense, the filaments are the actual collapse flow from the large to small scales: since the molecular cloud is formed by a compression (and because of its near-pressureless subsequent collapse), it is expected to have a sheet-like geometry, which fragments and further collapses into filaments. The filaments will accrete gas in a direction approximately perpen-

dicular to them and redirect the flow to their longitudinal direction, thus evacuating the filament. This flow around and along the filaments is shown in [Figure 1](#), reproduced from GV14. Those authors noticed that the above mentioned flow redirection happens smoothly, without shocks. This is possible, again, by the longitudinal evacuation of the accreted gas since a pressure excess simply increases the longitudinal flow rate. Additionally, those authors noticed that the filaments in their simulations appear to reach a steady state, so that they exist for times longer than their flow-crossing time.

Verification of this mode of filament structure and evolution may be achievable by exploiting the tools available in astrochemistry. Molecular line observations of known tracers of molecular cloud structure at sufficient sensitivity and spatial and spectral resolution can reveal various properties including the density and temperature (e.g., [Busquet et al. 2013](#); [Hacar et al. 2013](#); [Fehér et al. 2016](#); [Xiong et al. 2017](#); [Liu et al. 2018](#); [Sepúlveda et al. 2020](#); [Schmiedeke et al. 2021](#)), and velocity flow (or accretion rate) into and through the filament (e.g., [Lee et al. 2014](#); [Dhabal et al. 2018](#); [Guo et al. 2021](#); [Zhou et al. 2021](#)). To probe the accretion rate into the filament, one can exploit the chemical timescales of molecule formation from the diffuse to the dense interstellar medium. In contrast to an equilibrium state, a gas parcel falling into a filament experiences a changing physical environment. So, a given molecular species will trace the density distribution only if the molecule is able to form faster than the timescale at which the density and temperature changes. The abundance of a slow-forming molecule, in contrast, will lag behind the actual gas density of the parcel it is observed in. As a consequence, a filament observed using a fast-forming molecule should appear wider than the same filament observed using a slow-forming molecule. This change in the filament thickness when measured with different molecular lines should reflect the accretion rate that the filament experiences.

In this contribution, we explore the time-dependent molecular abundances in the accretion flow feeding a filament and contrast them with the abundances expected in a steady-state distribution. In [§2](#) we review the gas distribution model and the chemical network used. In [§3](#) we explore the resulting abundance distributions for a subset of the molecular species calculated, and explore the effect of changing the flow of mass towards the filament. Finally, in [§4](#) we present a discussion of the results.

2 FILAMENT MODEL

2.1 Physical model

2.1.1 Accreting, hydrodynamical model

GV14 analyzed two gaseous filaments formed in a simulation similar to one presented in [Vázquez-Semadeni et al. \(2007\)](#). They used the SPH code GADGET-2 to follow the evolution of two colliding streams of gas at a density and temperature similar to the warm neutral medium. The code was modified to include the cooling function proposed by [Koyama & Inutsuka \(2002\)](#) (with typographical errors corrected as outlined in [Vázquez-Semadeni et al. 2007](#)), so that the gas is thermally bistable. The streams move initially in opposite direc-

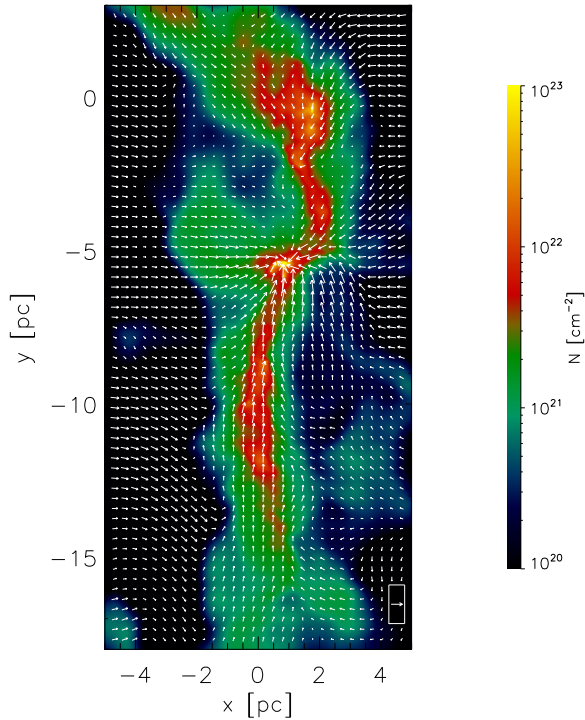


Figure 1. Filament 2 from GV14 (section of their fig. 3), at 26.56 Myr into their simulation. Colours show the column density of the gas, while the arrows show the density-weighted projected velocity, with the arrow in the lower right representing 2 km s^{-1} .

tions towards each other at $1.2 c_s$, where c_s is the adiabatic sound speed, inducing a phase transition to the cold neutral medium at the region where the flows collide. This dense layer accretes gas from the remnants of the initial flows, thus increasing its mass and ultimately reaching a density larger than $5 \times 10^4 M_\odot$. The resulting dense cloud is ram-pressure confined by the inflowing gas and it is therefore subjected to hydrodynamical instabilities (Vishniac 1994; Walder & Folini 2000; Heitsch et al. 2005, 2006; Vázquez-Semadeni et al. 2006). These instabilities create moderately supersonic turbulence within it and, in turn, induce non-linear density fluctuations. Although the layer’s mass increases in time and eventually becomes gravitationally unstable, the individual density enhancements collapse before the cloud as a whole. An important advantage of such a simulation setup is that the internal turbulence is generated in a self-consistent way, and so we do not need to impose a driving rate. Imposing this would carry the risk of over-driving the turbulent flow and artificially supporting the cloud against a global gravitational collapse. Additionally, the induced density fluctuations and *remnant* surrounding flow will also be consistent with one another. We refer the reader to Vázquez-Semadeni et al. (2007) for further details on the global evolution of the molecular cloud.

The filaments formed in this simulation are long-lived, being clearly discernible as long as there is enough gas falling into them. They appear to reach a steady state since the

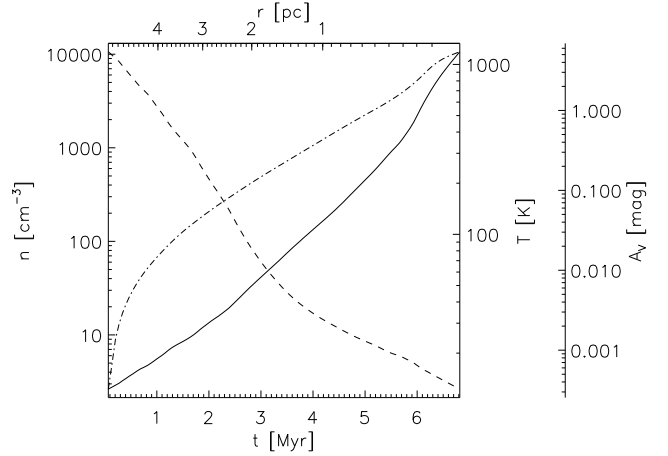


Figure 2. Density (*solid*), temperature (*dashed*), and visual extinction (*dash-dotted*) evolution of a gas parcel as it is accreted into the filament for the nominal accretion case (see §3). The physical conditions that the parcel experiences are plotted as a function of time and distance from the center of the filament.

accreted gas is evacuated along the filament onto clumps formed within the filament or at the position where two or more filaments meet, thus forming a hub-and-spoke distribution. GV14 report filament lengths of $\sim 15 \text{ pc}$, masses of $\sim 10^3 M_\odot$ (depending on the density threshold used to define the structures), a flattened density profile with a core size of $\sim 0.3 \text{ pc}$ and a power-law envelope with an approximately -2.5 logarithmic slope. The measured accretion rate toward the filament is $10 M_\odot \text{ pc}^{-1} \text{ Myr}^{-1}$ (also depending on the density threshold used to define it).

While being accreted, a gas parcel will experience an increasing density, decreasing temperature, and increasing visual extinction. By assuming that the filament is in steady state, we can use the azimuthally and longitudinally averaged radial velocity from GV14 to obtain the physical conditions a gas parcel experiences as a function of time (see Fig. 2). In this case, the density increases from ~ 3 to $\sim 10^4 \text{ cm}^{-3}$ in an approximately exponential form (with an e-folding time of about 0.83 Myr), the gas temperature decreases from $\sim 10^3$ to $\sim 10 \text{ K}$ and the visual extinction reaches a value of $\sim 5.4 \text{ mag}$ at the centre of the filament.

2.1.2 Non-accreting, static model

We consider two scenarios in this work: i) one in which we compute the chemical evolution of the parcel as it infalls into the filament, and ii) another in which we compute the chemical evolution as a function of time only at fixed positions along the flow (i.e., we decouple the chemistry from the flow). For this latter case, we consider the density and temperature distribution to be static in time, i.e., the filament does not accrete from its surroundings. Here, each gas parcel experiences the physical conditions shown in Figure 2 as a function of radius only (without the time dependence in the bottom axis). We note here that the chemistry is fully decoupled from the hydrodynamics, i.e., the chemical structure is calculated by post-processing the simulated physical

conditions resulting from the hydrodynamics simulations. We later discuss the implications of this assumption.

2.2 Chemical model

The chemical model used in this work is described in detail in [Walsh et al. \(2012\)](#) and [Walsh et al. \(2014\)](#) and we provide a brief description here. This model was originally developed for use in protoplanetary disks but is inherently flexible, and has been used in a variety of environments including the envelopes of forming protostars (e.g., [Drozdovskaya et al. 2014](#)), shocks in outflow cavity walls (e.g., [Palau et al. 2017](#)), dark clouds (e.g., [Penteado et al. 2017](#)), and the reaction network has also been used in models of circumstellar outflows (e.g., [Van de Sande et al. 2021](#)).

Because we are simulating the chemical evolution from the diffuse to the dense interstellar medium, it is necessary to include all competing chemical processes that lead to the key molecular tracers considered in this work which range from simple diatomics (e.g., CO and CN) to larger organic molecules (e.g., H₂CO and CH₃OH). For example, as the visual extinction and the density increase and the temperature decreases, freeze-out onto dust grains of abundant elements such as oxygen, begins to compete with gas-phase formation of simple molecules such as CO. The freeze-out of oxygen atoms eventually leads to the formation of water ice via grain-surface hydrogen-addition reactions (see, e.g., [van Dishoeck et al. 2013](#)). As the temperature decreases further ($\lesssim 25$ K) CO begins to also freeze-out which triggers the formation of larger molecules via atom-addition reactions forming molecules such as methanol (CH₃OH; see, e.g., [Linnartz et al. 2015](#)). At low temperatures, molecules can be returned to the gas phase by non-thermal mechanisms such as photodesorption (see, e.g., [Cuppen et al. 2017](#), and references therein); hence, the inclusion of ice formation and ice chemistry also requires the need to include all possible mechanisms for ice destruction. As explained in the review of molecular cloud chemistry by [Agúndez & Wakeham \(2013\)](#), such large chemical networks are highly non-linear and stiff and specialised solvers are required (e.g., ODEPACK¹). This is also the motivation for decoupling the chemistry from the physics and computing the chemistry in a post-processing manner. It remains computationally demanding to couple comprehensive chemistry networks with hydrodynamics simulation with modern attempts limited to reduced networks simulating the chemistry of simple species only (see, e.g., [Haworth et al. 2016](#), for the case study of protoplanetary disks but the discussion of which is generally applicable).

The model includes gas-phase chemistry based on the Rate12 version of the UMIST Database for Astrochemistry (UDfA²; [McElroy et al. 2013](#)), supplemented with gas-grain chemistry derived from the OSU 2008 chemical network ([Garrod et al. 2008](#); [Laas et al. 2011](#)). We include self- and mutual-shielding of H₂, CO, and N₂ to photodissociation by interstellar photons using the shielding functions from [Heays et al. \(2017\)](#). The gas-grain processes included are freeze-out onto dust grains, and desorption (sublimation) into the

gas-phase via thermal desorption, photodesorption by both external UV photons and by secondary UV photons induced by the interaction of cosmic rays with molecular hydrogen, and reactive desorption. The binding energies needed to calculate the thermal desorption rates (and grain-surface reaction rates) are those compiled for use with UDfA. We used laboratory-measured photodesorption rates where available. We also include grain-surface reactions to allow the formation and processing of ices on dust grains. These reactions include atom-addition reactions, radical-radical recombination, and photodissociation of ices. The reaction rates for gas-grain processes are calculated according to the prescriptions recommended in [Cuppen et al. \(2017\)](#). We adopt a two-phase model in this work, i.e., we do not discriminate between chemistry occurring in the bulk ice and that occurring on the surface of the ice mantles. However, we do restrict that active grain-surface chemistry occurs within two monolayers only in the ice mantle. We include the formation of molecular hydrogen via the grain-surface recombination of atomic hydrogen.

Because the filament evolution starts with a high temperature, low density, and low A_V , i.e., conditions representative of the diffuse interstellar medium, we begin the chemistry with atomic initial conditions using the abundances presented in [Table 1](#) and that are reproduced from [McElroy et al. \(2013\)](#), the only difference being that we assume here that all hydrogen is initially in atomic form. The abundances correspond to the values measured for the elemental composition of the local diffuse interstellar medium in the Milky Way and account for depletion of heavy elements (i.e., metals) onto refractory dust grains ([Graedel et al. 1982](#)). The chemical evolution of the filament is calculated over the averaged physical conditions presented in [Fig. 2](#). In this way we follow the formation of molecules along a typical parcel of gas falling into the filament that experiences an increasing density and A_V and a decreasing temperature. Note that most molecular formation under these conditions occurs via gas-phase chemistry; gas-grain and grain-surface processes only begin to become important once the A_V increases to $\gtrsim 3$ mag, and the temperature falls below ~ 100 K, at which point atoms like atomic oxygen begin to stick to dust grains and the formation of water ice begins as described above.

One caveat in our adopted methodology is that we assume that the dust and gas temperatures are equal along the flow. In reality these temperatures will decouple at low density in irradiated clouds due to the competition between gas heating and cooling (see, e.g., [Hollenbach & Tielens 1999](#)). Hence, our simulations are not self-consistent in that the physics and chemistry of the filament are decoupled; however, this assumption is necessary in order to include the level of chemical complexity needed to simulate all possible observable molecular tracers considered in this work.

For the nominal, accreting filament scenario, the chemical evolution is computed in the changing physical conditions shown in [Figure 2](#). For the non-accreting case, the chemical evolution is calculated at fixed conditions for a time of 63 Myr which should be sufficiently long for the gas-phase abundances to reach steady state across the filament. We do this to test if the formation timescale of molecules can be used as a diagnostic of the flow rate into the filament.

¹ <https://computing.llnl.gov/projects/odepack/software>

² <http://www.udfa.net>

Table 1. Initial elemental abundances (with respect to total H nuclei) from [McElroy et al. \(2013\)](#).

Species	Fractional abundance
H	1.00
He	9.75×10^{-2}
O	3.20×10^{-4}
C	1.40×10^{-4}
N	7.50×10^{-5}
S	8.00×10^{-8}
F	2.00×10^{-8}
Si	8.00×10^{-9}
Mg	7.00×10^{-9}
Cl	4.00×10^{-9}
Fe	3.00×10^{-9}
P	3.00×10^{-9}
Na	2.00×10^{-9}

3 ABUNDANCES

A molecule with a short chemical timescale, i.e. a fast-forming molecule, will reach its steady-state abundance before the gas parcel’s environment changes significantly. In this case, the given molecular abundance will accurately reflect the local physical conditions within the filament. In contrast, a molecule with a long chemical timescale, i.e. a slow-forming molecule, will not reach its steady-state abundance before the gas parcel falls more deeply into the filament and its environmental conditions change. In this case, the slow-forming molecule abundance *will not* reflect the filament density and temperature. Therefore, steady-state and time-dependent abundances will differ for slow-forming molecules, although the interdependencies of the formation rates of the molecular species means that the abundance of fast-forming molecules will also differ. Both cases are shown in Figure 3.

The top panels of Fig. 3 show the fractional abundances of several common and observable molecular tracers of cold and dense gas for the case in which the chemistry onto the filament is calculated along the accretion flow (i.e., the chemistry and flow are coupled). The distance along the flow at which a molecule reaches an appreciable gas-phase fractional abundance ($\gtrsim 10^{-11}$) varies between $\sim 1-2$ pc for molecules such as CO, CN, C₂H (formed the farthest out), HCN, HNC, and NH₃, and $\sim 0.2-0.9$ pc for other species considered here including larger molecules such as H₂CO, H₂CS, HC₃N, and CH₃OH (formed the farthest in). This structure mimics to some extent the chemical structure predicted by chemical models of weak to moderate photon-dominated regions (see, e.g., the recent models of the chemical structure of the Horsehead nebula by [Le Gal et al. 2017](#)). In these models, radicals such as CN and C₂H sit closer to the edge of the cloud than chemically-related molecules such as HCN and c-C₃H₂, respectively. Large molecules such as CH₃OH take longer to form along the flow due to their reliance on grain-surface chemistry. For instance, CH₃OH can only form after the gas-phase formation of CO. Once the temperature is sufficiently low, CO can begin to stick to grain surfaces where it is hydrogenated to form H₂CO and CH₃OH. H₂CO and CH₃OH are then returned to the gas-phase via non-thermal

desorption, in this case, via a combination of photodesorption and reactive desorption.

The bottom panels of Fig. 3 show the fractional abundances of the same molecules for the case where the chemistry is computed in time only, i.e., the chemistry and flow are decoupled. The general pattern described above still persists; however, there are some differences. The larger molecules (HC₃N, H₂CS, and CH₃OH) now only reach appreciable abundances ($\gtrsim 10^{-11}$) much farther into the filament (~ 0.1 pc). As the chemistry here is close to steady-state, the results show that the destruction timescale of these species at distances beyond ~ 0.1 pc are shorter than 63 Myr. The most profound difference is in the composition of the gas entering the densest point of the filament. Several species have fractional abundances that differ by more than an order of magnitude between the two cases. The CN and C₂H fractional abundances are higher in the static case compared with the accreting case by one and two orders of magnitude, respectively. This is due to the long timescales required for cosmic-ray reactions to occur in dense gas, which can ionise helium, which goes on to dissociate and ionise molecules, creating radicals. Further, the H₂CO and CH₃OH fractional abundances are lower in the static case by around two orders of magnitude at the same point. This is again due to the long timescales needed to destroy molecules via cosmic-ray reactions. Whilst in the coupled case, most of the fractional abundances increase monotonically along the flow (with the exception of the radicals CN and C₂H), the abundances in the static case show more complex morphologies along the filament, with many species having a double-peaked abundance structure. For instance, C₂H exhibits a peak in abundance at ≈ 0.5 pc in the static case, that is mirrored by the chemically-related species, c-C₃H₂, and there is a similar behaviour in the case of CN, HCN, HNC, and HC₃N.

The abundance behaviour described above along with the results shown in Fig. 3 show that the formation (and destruction) timescale of all considered molecules are indeed longer than the time spent at each location along the flow.

That is, we have demonstrated that the chemistry along the flow is not at steady state. Hence, the accretion towards the filament implies that slow-forming molecules will not reach their chemical timescale until later times, corresponding to regions closer to the filament crest, and in the accreting case we should expect, as a first approximation, narrower distributions for slow-forming molecules compared to the distributions of fast-forming molecules.

The complicated distribution of abundances makes the width at a given threshold abundance an unreliable measure of the accretion effect on the molecular chemistry. A simple analytical function fitting would also be of little use. Instead, we measured the abundance widths using the full-width at half maximum (fwhm) of the projected column density distribution convolved with a Gaussian profile with 0.1 pc size, as this would better reflect an astronomical observation. The resulting smoothed abundance distributions are available as a supplementary online figure and the corresponding width values for selected molecules are shown in Figure 4.

An important aspect of the adopted model filament is the redirection of the accretion toward the filament to longitudinal flow (see §1). This longitudinal evacuation of

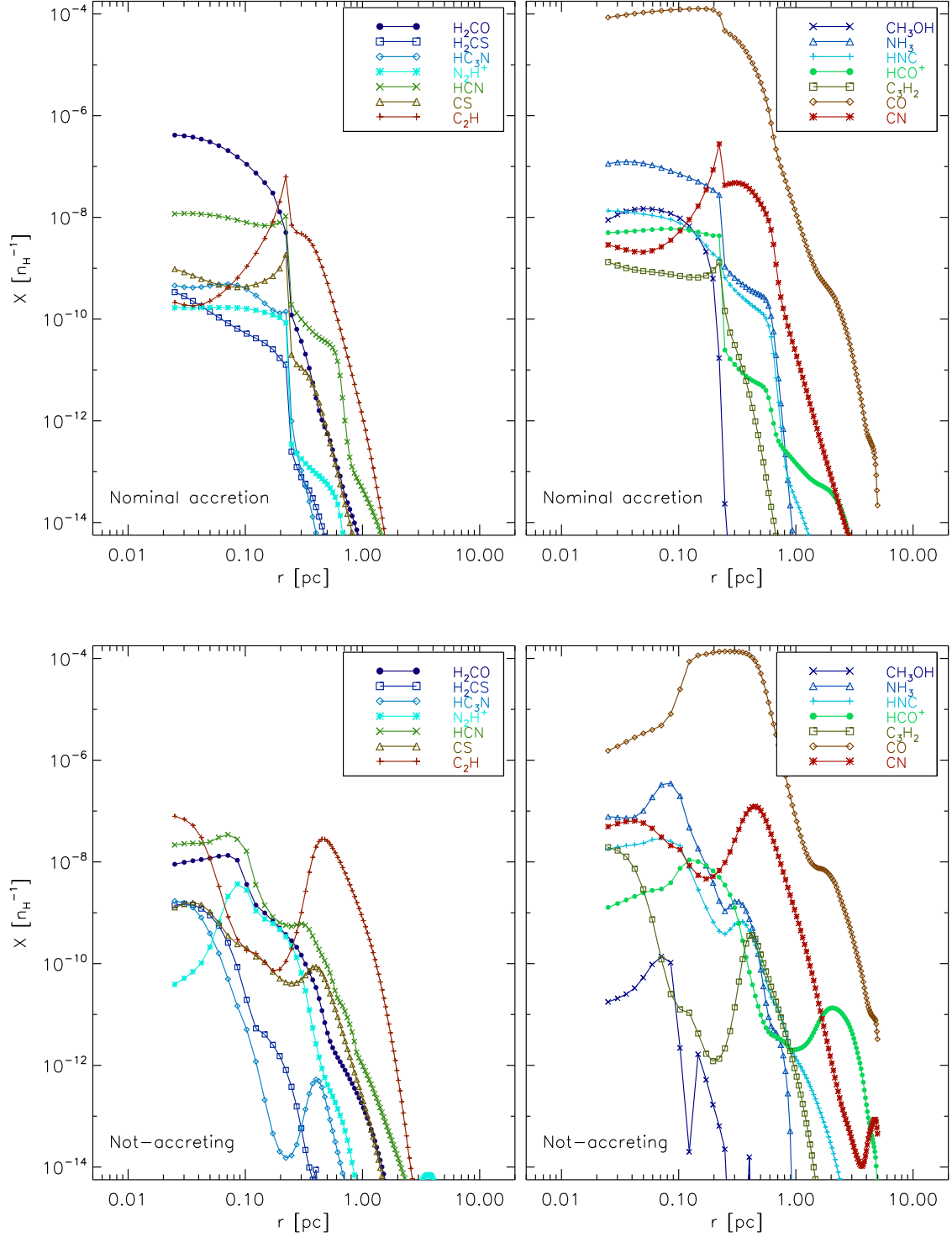


Figure 3. Time dependent (i.e. accreting case, *top row*) and steady state molecular abundances (non-accreting case, *bottom row*) for a set of molecular species. Differences between both abundance distributions reflect the changing density and temperature environment for molecules with slow chemical timescales.

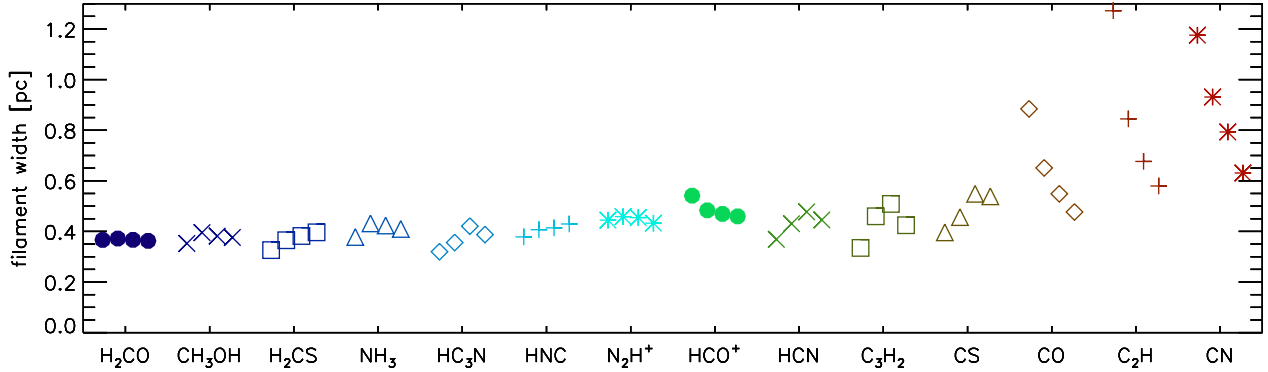


Figure 4. Filament width measured as the full-width at half maximum for the convolved, projected molecular abundance distributions. Data points for each molecular species correspond to, from left to right, the steady state, half the accretion rate, nominal accretion, and twice the accretion rate cases. Colours and symbols are the same as in Fig. 3.

gas adds a degree of freedom to the conservation of mass, namely the mass flux along the filament. Since the continuity equation in steady state is linear in the velocity, we may multiply the radial and longitudinal velocities by a constant factor and retain the same density profile. Although a fully self-consistent model for the density and velocity structure of the filament is beyond the scope of this contribution (Gómez & Vázquez-Semadeni, *in prep.*), here we increase (or decrease) the radial velocity of the flow in order to emulate different accretion rates. These new radial velocities will imply that a gas parcel experiences a more rapidly (or more slowly) changing environment, yielding different molecular abundance profiles.

GV14 reported an accretion rate to the filament of $10 M_{\odot} \text{ pc}^{-1} \text{ Myr}^{-1}$. Together with the static model and this nominal accretion rate, Fig. 4 shows the calculated fwhm values for cases with double and half the nominal accretion rate. Widths measured for the C_2H , CN, and CO molecules are the most sensitive to the changing accretion toward the filament, with thinner distributions as the accretion rate increases. On the other hand, widths for some other molecules like N_2H^+ and H_2CO , remain almost constant for different accretion rates. Yet other width values, like those for CS, HNC, and H_2CS , follow the opposite trend, with the molecule distribution growing wider with increasing accretion rate, although only marginally (for the density profile used here). For other molecules, like C_3H_2 and HCN, the corresponding width values show a non-monotonic dependence on accretion rate.

4 DISCUSSION

4.1 Molecule pairs tracing accretion onto filaments

In the GHC scenario, filaments represent the locus of gas accretion from the cloud to the star-forming clumps. Therefore, the filaments are not density but flow structures as the gas within them is constantly replenished. This means that a gas parcel within the filament will experience changing

Table 2. Molecular species ordered by increasing sensitivity to accretion.

	Molecule	w_{nominal} [pc]	$w_{\text{nominal}}/w_{\text{static}}$
Insensitive to accretion	H_2CO	0.37	1.00
	N_2H^+	0.45	1.02
	CH_3OH	0.38	1.08
	HNC	0.41	1.09
	NH_3	0.42	1.12
	HCO^+	0.47	0.87
Marginally sensitive	H_2CS	0.38	1.17
	HCN	0.48	1.29
	HC_3N	0.42	1.32
Sensitive to accretion	CS	0.55	1.38
	CN	0.79	0.67
	C_3H_2	0.51	1.52
	CO	0.55	0.62
	C_2H	0.68	0.53

densities, temperatures, and opacities, at a rate depending on the accretion rate toward the filament. Since chemical abundances depend on these physical conditions, molecular distributions should reflect the accretion. Furthermore, the chemical timescales will be convolved with the accretion timescale, so that faster-forming molecules will better reflect the *local* physical conditions a gas parcel experiences than slower-forming ones, which will retain memory of the density and temperature external to the actual position of the gas parcel.

In this contribution, we propose that the widths measured using different molecular species can be used to measure the accretion toward the filament. In our Figure 4, we show that the distribution of some molecules such as CN, C_2H , CO, or HCO^+ becomes narrower with increasing accretion rate, while other molecules present the opposite behavior (e.g., CS), and other molecules do not change their width under any circumstances (H_2CO , CH_3OH , NH_3). Fig-

ure 4 actually presents the molecules ordered with increasing filament width for the nominal accreting case. As can be seen from the figure, the molecules presenting smaller filament widths are also the molecules less sensitive to the different accretion rates. On the contrary, molecules with largest filament widths are also those most sensitive to accretion. This suggests that the formation of the group of ‘insensitive’ molecules probably requires a particular density/temperature threshold and that the filament width simply indicates the width at which these physical conditions are reached, no matter the accretion history, and that the formation of the group of molecules sensitive to accretion is intimately related to the actual physical conditions of the gas.

In order to quantify this a little bit more, in Table 2 we present the subset of the molecular species considered in this work, ordered by sensitivity to the accretion rate.³ The table shows that, as suggested already in Fig. 4, our subset of molecules can be divided in two opposite groups, mainly the molecules ‘insensitive’ to accretion, such as N_2H^+ , H_2CO , CH_3OH , NH_3 , and the molecules ‘sensitive’ to accretion such as CS, CN, C_2H , CO, and C_3H_2 . We classify a molecule as ‘insensitive’ to accretion if the variation of its filament width with respect to the static case (in logarithmic scale) is smaller than $\sim 10\%$, while those molecules with variations larger than $\sim 40\%$ will be considered as molecules ‘sensitive’ to accretion. Note that some of the ‘sensitive’ molecules have also been classified in previous works such as ‘early-time’ molecules (e.g., Taylor et al. 1998) or molecules tracing diffuse cores (e.g., Frau et al. 2012), while the ‘insensitive’ molecules have been classified as ‘late-time’ or tracing ‘deuterated cores’. However, the exact correspondence with previous works might not be perfect because, for example, here we do include grain-phase reactions which were not included by Taylor et al. (1998).

The sensitivity to accretion rate may be (marginally) increased if we consider width ratios for pairs of molecular species. Figure 5 shows the width ratios of CN and C_2H to CS as a function of accretion rate to the filament. Although these ratios change by a factor of a few for the range of accretion considered, there is a clear trend of decreasing width ratio of CN, C_2H , and CO to CS with increasing accretion. As can be seen from Figure 5, for large accretion rates the widths of the ‘insensitive’ molecules tend to be the same and this might not be a strong test from an observational point of view. Thus, it might be also useful to study the width ratios between sensitive and insensitive molecules. For example, the width ratio of NH_3 to CS, or the width ratio of N_2H^+ to CS should be smaller than one (CS should be always broader) for high accretion rates.

The results presented in Fig. 5 indicate that observations of filaments with different molecular tracers could be a powerful tool to provide evidence of on-going accretion onto the filaments, if the appropriate tracers are used. In this sense, the observational work of Gong et al. (2018) can provide a first test to the model developed here. These authors observed multiple transitions in the Serpens filament using

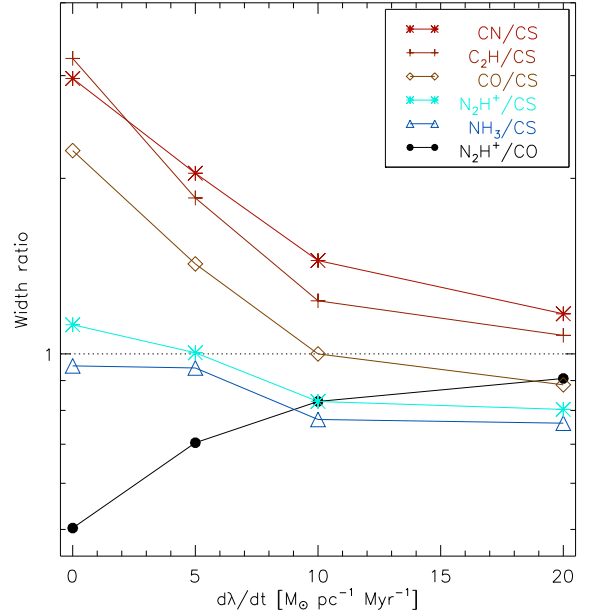


Figure 5. Filament width ratios for CN, C_2H , CO, N_2H^+ , and NH_3 to CS as a function of accretion rate to the filament. Colours and symbols for these molecular species correspond to those in Fig. 3. N_2H^+ to CO width ratio is also shown.

the Purple Mountain Observatory with a beam of about $50''$, inferring a linear mass density of $36\text{--}41 M_{\odot} \text{ pc}^{-1}$, fully consistent with the linear mass density of the filaments of the GV14 simulations (of $\sim 40 M_{\odot} \text{ pc}^{-1}$). Gong et al. (2018) also measure the radial accretion rate onto the filament to be about $45 M_{\odot} \text{ pc}^{-1} \text{ Myr}^{-1}$, only a factor of two larger than the accretion rate measured in the simulations of GV14, and similar to the accretion rate estimated by Palmeirim et al. (2013) and Shimajiri et al. (2019) in the Taurus main filament. Judging from Fig. 5 and given the radial accretion rate measured in the Serpens filament, one would expect a width ratio of N_2H^+ to CS of about 0.8 and interestingly the fwhm of the CS distribution presented in Fig. 2 of Gong et al. (2018) is 50% larger than the N_2H^+ distribution, yielding a width ratio of N_2H^+ to CS of 0.7, very close to the value predicted in our model. However, opacity effects must be affecting the CS observations. Gong et al. (2018) also present abundance maps of C^{18}O and N_2H^+ . From Fig. 6 of Gong et al. (2018) we estimate a width ratio of N_2H^+ to C^{18}O of about 0.7. By comparing this value to the ratio shown in Fig. 5 of N_2H^+ to CO (the behavior of C^{18}O should be very close to that of CO), we infer an approximate accretion rate of about $5 M_{\odot} \text{ pc}^{-1} \text{ Myr}^{-1}$, assuming that the Serpens filament is similar to the filament taken from GV14. Although accurate works specifically designed to test this model should be carried out, the study of Gong et al. (2018) already constitutes a first test suggesting chemical differentiation due to accretion onto filaments.

4.2 Caveats of the model

C_2H and CN are molecular species that are sensitive to the

³ Measured as the absolute value of the logarithm of the ratio of filament widths measured for the nominal accretion to the static models.

surrounding radiation field. So, it could be argued that the effect discussed here, if observationally verified, could be due to filaments embedded in different radiation fields. In order to test this, we calculated the molecular abundances for the nominal accretion, for weaker (a factor of 0.3) and stronger ($\times 3$ and $\times 10$) radiation fields. Although C_2H and CN abundances indeed change, the measured widths decrease only 80%, while other molecule distributions become narrower by a similar amount. More importantly, the CN to CS and C_2H to CS ratios remain relatively constant since almost all molecular species also grow narrower with increasing radiation field.

For this study we used a specific filament density and velocity profile, namely the profile reported by GV14 for a simulation of a molecular cloud undergoing large-scale, hierarchical gravitational collapse. GV14 fitted a Plummer profile with a core-radius of 0.11 pc for this filament's volume density distribution, although the column density distribution is better fitted by a 0.31 pc core radius. The corresponding fwhm for the column density distribution used here is 0.47 pc, similar to the values obtained for every molecule, with exception of C_2H and CN, which are the most sensitive to accretion rate. This is not surprising since the molecular abundances relate in a complex fashion to the ambient density, even more with a dynamically changing density.

Real filaments are not cylindrically symmetric. Observations of filamentary structures in various molecular tracers frequently show elongated, velocity coherent, fiber-like substructures (Hacar et al. 2013, for example, but see also Zamora-Avilés et al. 2017). In the GHC scenario, these fibers may be seen as part of the large scale collapse, and so, the fibers will also be accreting from their environment, although at different density and accretion regimes to the ones explored in the model used here. The effect described here, that different molecular tracers might yield different observed filament widths, should also happen at the fiber level. Models exploring this in a variety of self-consistent flow conditions, including the lack of axial symmetry (Naranjo-Romero et al. 2020), will be explored in a future contribution.

As mentioned, the main characteristic of the flow around the filament is that the velocity smoothly turns from radial to longitudinal, so that an accreted gas parcel slows down from supersonic to subsonic velocities without the need of a shock. In contrast, in the turbulent-compression model, filaments appear at the positions where flows meet and so we would expect to find shocked gas around the filament, with high abundances of typical shock tracers such as SiO or CH_3OH at the locus where the velocity turns from radial to longitudinal. Although widespread SiO and CH_3OH emission has been found in some filamentary clouds (e.g., Jiménez-Serra et al. 2010; Duarte-Cabral et al. 2014; Louvet et al. 2016; Cosentino et al. 2018; Li et al. 2020; Liu et al. 2020; Zhu et al. 2020), the turbulent-compression model requires to find them at high velocities, while these shock tracers have been found associated with narrow linewidths of $1-6 \text{ km s}^{-1}$. The presence of a shock at the filament border should have an impact on the chemical abundances, and detailed studies of shock tracers in the filament surroundings could be crucial to distinguish these scenarios.

In the GHC scenario, the thermodynamic behavior of the gas around molecular filaments should have little effect

on the gas dynamics since the gravitational collapse occurs in an almost pressureless fashion. Still, Micic et al. (2013) showed that the choice of cooling function might change the cloud morphology resulting in the simulation as slower cooling, shock-heated gas yields overpressured regions that expand against the thermal-instability induced flow. Since the filament model under consideration corresponds to a later time, when gravitational instability drives the gas flow, the details of the cooling function should not have a large impact on our conclusions, but should be taken into consideration for models of filaments formed in the gravoturbulent scenario. The simulations discussed by Micic et al. (2013) show that using the cooling function from Koyama & Inutsuka (2002, as GV14 did) yields dense regions that are $\sim 10 \text{ K}$ colder than their equivalent when the time-dependent cooling from Glover & Mac Low (2007a,b) is used. With this in mind, we artificially increased the gas temperature by 10 K in the filament model and repeated the calculation of filament width ratios for the static and nominal accretion cases. We found that the ratios shown in Table 2 change by an average of 2%, which would be relevant only for molecular species that we classified as insensitive to accretion.

Finally, we note that we have post-processed the chemical evolution, i.e., we have decoupled the complex chemistry from the physical simulation. A fully self-consistent model would use the abundances from a coupled chemical model to compute the heating and cooling rates on the fly, and indeed this has been done but using reduced networks only (see, e.g., Hocuk et al. 2016, for an example with simplified grain-surface chemistry). Such simplified networks focus on computing the abundances of key heating species and coolants at the expense of chemical complexity; however, we are interested in the abundances of key observables at sub-mm wavelengths which require much more complex networks in order to accurately (in as much as is possible) simulate their chemical evolution. However, it is worth to check if the results of the chemical simulations are consistent with the assumptions made in the heating and cooling functions used in GV14. The volatiles involved in the heating and cooling rates are H_2 and CO, and atomic and ionic lines of CII, OI, FeII, and SiII (Koyama & Inutsuka 2000). Figure 1 in that work shows that at densities between $\sim 1 \text{ cm}^{-3}$ and $\sim 10^4 \text{ cm}^{-3}$ (relevant for this work) OI, CII, and CO are the primary coolants, and H_2 formation/destruction is a primary heating source. Koyama & Inutsuka (2000) adopt elemental abundances of 4.6×10^{-4} and 3.0×10^{-4} for O and C, respectively. These values are similar to our assumed initial abundances shown in Table 1, albeit slightly higher. Hence the cooling rates would be expected to be slightly lower in a self-consistent version of our model although this slight change should not drastically change the gas temperature. We note that our H_2 and CO abundance profiles with density differ from those presented in figure 1 of Koyama & Inutsuka (2000) in that we find molecular formation takes place at lower densities because we have a higher shielding column ($> 10^{21} \text{ cm}^{-2}$) than simulated in that work ($10^{19} - 10^{20} \text{ cm}^{-2}$). This is expected to increase the gas temperature at low densities due to increased heating provided by H_2 ; indeed, we find that is the case and at a density of $\sim 10 \text{ cm}^{-3}$ Koyama & Inutsuka (2000) find a gas temperature of $\sim 100 \text{ K}$ whereas the gas temperature in the filament at this density is $\approx 300 \text{ K}$. Hence, we conclude

that the physical structure of the simulated filament should not be significantly affected by the decoupling of the hydrodynamics and chemistry; however, future simulations would be needed to fully quantify the differences.

The relation between widths measured for different molecules and accretion presented in Figs. 4 and 5 is specific to the filament discussed in GV14. While a fully self-consistent model of an accreting filament is beyond the scope of this contribution, these results show a promising way to verify and measure accretion rates towards molecular filaments and it could be applicable to other prestellar objects that may be modeled as out of equilibrium structures.

ACKNOWLEDGEMENTS

We thank E. Vázquez-Semadeni, J. Ballesteros-Paredes, and an anonymous referee for useful comments and suggestions. G.C.G. acknowledges financial support from the UNAM-PAPIIT IN103822 grant. A.P. acknowledges financial support from the UNAM-PAPIIT IN111421 grant, and from the CONACyT project number 86372 of the ‘Ciencia de Frontera 2019’ program, entitled ‘Citlalcóatl: A multiscale study at the new frontier of the formation and early evolution of stars and planetary systems’, México. A.P. and G.C.G. acknowledge support from CONACyT’s Sistema Nacional de Investigadores. C.W. acknowledges financial support from the University of Leeds, the Science and Technology Facilities Council, and UK Research and Innovation (grant numbers ST/T000287/1 and MR/T040726/1).

DATA AVAILABILITY

The data underlying this article will be shared on reasonable request to the corresponding author.

REFERENCES

- Agúndez M., Wakelam V., 2013, *Chemical Reviews*, **113**, 8710
- André P., Di Francesco J., Ward-Thompson D., Inutsuka S. I., Pudritz R. E., Pineda J. E., 2014, in Beuther H., Klessen R. S., Dullemond C. P., Henning T., eds, *Protostars and Planets VI*. p. 27 ([arXiv:1312.6232](https://arxiv.org/abs/1312.6232)), [doi:10.2458/azu_uapress_9780816531240-ch002](https://doi.org/10.2458/azu_uapress_9780816531240-ch002)
- Arzoumanian D., et al., 2021, *A&A*, **647**, A78
- Auddy S., Basu S., Kudoh T., 2016, *ApJ*, **831**, 46
- Balsara D., Ward-Thompson D., Crutcher R. M., 2001, *MNRAS*, **327**, 715
- Bonne L., et al., 2020, *A&A*, **644**, A27
- Burge C. A., Van Loo S., Falle S. A. E. G., Hartquist T. W., 2016, *A&A*, **596**, A28
- Busquet G., et al., 2013, *ApJ*, **764**, L26
- Chen H.-R. V., et al., 2019, *ApJ*, **875**, 24
- Chen C.-Y., Mundy L. G., Ostriker E. C., Storm S., Dhabal A., 2020a, *MNRAS*, **494**, 3675
- Chen M. C.-Y., et al., 2020b, *ApJ*, **891**, 84
- Chung E. J., et al., 2021, *arXiv e-prints*, p. [arXiv:2106.03897](https://arxiv.org/abs/2106.03897)
- Cosentino G., et al., 2018, *MNRAS*, **474**, 3760
- Cuppen H. M., Walsh C., Lamberts T., Semenov D., Garrod R. T., Penteado E. M., Ioppolo S., 2017, *Space Sci. Rev.*, **212**, 1
- Dewangan L. K., Ojha D. K., Sharma S., Palacio S. d., Bhaduri N. K., Das A., 2020, *ApJ*, **903**, 13
- Dhabal A., Mundy L. G., Rizzo M. J., Storm S., Teuben P., 2018, *ApJ*, **853**, 169
- Dobashi K., Shimoikura T., Ochiai T., Nakamura F., Kamenno S., Mizuno I., Taniguchi K., 2019, *ApJ*, **879**, 88
- Drozdovskaya M. N., Walsh C., Visser R., Harsono D., van Dishoeck E. F., 2014, *MNRAS*, **445**, 913
- Duarte-Cabral A., Bontemps S., Motte F., Gusdorf A., Csengeri T., Schneider N., Louvet F., 2014, *A&A*, **570**, A1
- Fehér O., Tóth L. V., Ward-Thompson D., Kirk J., Kraus A., Pelkonen V. M., Pintér S., Zahorecz S., 2016, *A&A*, **590**, A75
- Fernández-López M., et al., 2014, *ApJ*, **790**, L19
- Fischera J., Martin P. G., 2012, *A&A*, **542**, A77
- Frau P., Girart J. M., Beltrán M. T., 2012, *A&A*, **537**, L9
- Garrod R. T., Widicus Weaver S. L., Herbst E., 2008, *ApJ*, **682**, 283
- Glover S. C. O., Mac Low M.-M., 2007a, *ApJS*, **169**, 239
- Glover S. C. O., Mac Low M.-M., 2007b, *ApJ*, **659**, 1317
- Gómez G. C., Vázquez-Semadeni E., 2014, *ApJ*, **791**, 124
- Gómez G. C., Vázquez-Semadeni E., Zamora-Avilés M., 2018, *MNRAS*, **480**, 2939
- Gong Y., Li G. X., Mao R. Q., Henkel C., Menten K. M., Fang M., Wang M., Sun J. X., 2018, *A&A*, **620**, A62
- Gong Y., Belloche A., Du F. J., Menten K. M., Henkel C., Li G. X., Wyrowski F., Mao R. Q., 2021, *A&A*, **646**, A170
- Graedel T. E., Langer W. D., Frerking M. A., 1982, *ApJS*, **48**, 321
- Guo W., et al., 2021, *ApJ*, **921**, 23
- Hacar A., Tafalla M., Kauffmann J., Kovács A., 2013, *A&A*, **554**, A55
- Hacar A., Tafalla M., Forbrich J., Alves J., Meingast S., Grossschedl J., Teixeira P. S., 2018, *A&A*, **610**, A77
- Haworth T. J., et al., 2016, *Publ. Astron. Soc. Australia*, **33**, e053
- Heays A. N., Bosman A. D., van Dishoeck E. F., 2017, *A&A*, **602**, A105
- Heitsch F., 2013a, *ApJ*, **769**, 115
- Heitsch F., 2013b, *ApJ*, **776**, 62
- Heitsch F., Burkert A., Hartmann L. W., Slyz A. D., Devriendt J. E. G., 2005, *ApJ*, **633**, L113
- Heitsch F., Slyz A. D., Devriendt J. E. G., Hartmann L. W., Burkert A., 2006, *ApJ*, **648**, 1052
- Hennebelle P., André P., 2013, *A&A*, **560**, A68
- Hennebelle P., Pérault M., 1999, *A&A*, **351**, 309
- Henshaw J. D., Caselli P., Fontani F., Jiménez-Serra I., Tan J. C., 2014, *MNRAS*, **440**, 2860
- Hocuk S., Cazaux S., Spaans M., Caselli P., 2016, *MNRAS*, **456**, 2586
- Hollenbach D. J., Tielens A. G. G. M., 1999, *Reviews of Modern Physics*, **71**, 173
- Hu B., et al., 2021, *ApJ*, **908**, 70
- Inutsuka S.-I., Miyama S. M., 1992, *ApJ*, **388**, 392
- Issac N., Tej A., Liu T., Varricatt W., Vig S., Ishwara Chandra C. H., Schultheis M., 2019, *MNRAS*, **485**, 1775
- Jiménez-Serra I., Caselli P., Tan J. C., Hernandez A. K., Fontani F., Butler M. J., van Loo S., 2010, *MNRAS*, **406**, 187
- Kirk H., Myers P. C., Bourke T. L., Gutermuth R. A., Hedden A., Wilson G. W., 2013, *ApJ*, **766**, 115
- Koyama H., Inutsuka S.-I., 2000, *ApJ*, **532**, 980
- Koyama H., Inutsuka S.-i., 2002, *ApJ*, **564**, L97
- Laas J. C., Garrod R. T., Herbst E., Widicus Weaver S. L., 2011, *ApJ*, **728**, 71
- Le Gal R., Herbst E., Dufour G., Gratier P., Ruaud M., Vidal T. H. G., Wakelam V., 2017, *A&A*, **605**, A88
- Lee K. I., et al., 2014, *ApJ*, **797**, 76
- Li S., et al., 2020, *ApJ*, **903**, 119
- Lin C. C., Mestel L., Shu F. H., 1965, *ApJ*, **142**, 1431
- Linnartz H., Ioppolo S., Fedoseev G., 2015, *International Reviews in Physical Chemistry*, **34**, 205
- Liu H.-L., Stutz A., Yuan J.-H., 2018, *MNRAS*, **478**, 2119

- Liu T., et al., 2020, *MNRAS*, 496, 2790
- Liu X.-L., Xu J.-L., Wang J.-J., Yu N.-P., Zhang C.-P., Li N., Zhang G.-Y., 2021, *A&A*, 646, A137
- Louvet F., et al., 2016, *A&A*, 595, A122
- Lu X., et al., 2018, *ApJ*, 855, 9
- McElroy D., Walsh C., Markwick A. J., Cordiner M. A., Smith K., Millar T. J., 2013, *A&A*, 550, A36
- Micic M., Glover S. C. O., Banerjee R., Klessen R. S., 2013, *MNRAS*, 432, 626
- Molinari S., et al., 2010, *A&A*, 518, L100
- Naranjo-Romero R., Vázquez-Semadeni E., Loughnane R. M., 2020, arXiv e-prints, p. arXiv:2012.12819
- Ostriker J., 1964, *ApJ*, 140, 1056
- Padoan P., Juvela M., Goodman A. A., Nordlund Å., 2001, *ApJ*, 553, 227
- Palau A., et al., 2017, *MNRAS*, 467, 2723
- Palau A., et al., 2021, *ApJ*, 912, 159
- Palmeirim P., et al., 2013, *A&A*, 550, A38
- Penteado E. M., Walsh C., Cuppen H. M., 2017, *ApJ*, 844, 71
- Peretto N., et al., 2013, *A&A*, 555, A112
- Peretto N., et al., 2014, *A&A*, 561, A83
- Pillai T. G. S., et al., 2020, *Nature Astronomy*, 4, 1195
- Planck Collaboration et al., 2016, *A&A*, 586, A135
- Qiu K., Zhang Q., Menten K. M., Liu H. B., Tang Y.-W., 2013, *ApJ*, 779, 182
- Ren Z., et al., 2021, *MNRAS*, 505, 5183
- Schmiedeke A., et al., 2021, *ApJ*, 909, 60
- Schwörer A., et al., 2019, *A&A*, 628, A6
- Sepúlveda I., et al., 2020, *A&A*, 644, A128
- Shimajiri Y., André P., Palmeirim P., Arzoumanian D., Bracco A., Könyves V., Ntormousi E., Ladjelate B., 2019, *A&A*, 623, A16
- Stodólkiewicz J. S., 1963, *Acta Astron.*, 13, 30
- Tackenberg J., et al., 2014, *A&A*, 565, A101
- Tafalla M., Hacar A., 2015, *A&A*, 574, A104
- Taylor S. D., Morata O., Williams D. A., 1998, *A&A*, 336, 309
- Treviño-Morales S. P., et al., 2019, *A&A*, 629, A81
- Van de Sande M., Walsh C., Millar T. J., 2021, *MNRAS*, 501, 491
- Vázquez-Semadeni E., Ryu D., Passot T., González R. F., Gazol A., 2006, *ApJ*, 643, 245
- Vázquez-Semadeni E., Gómez G. C., Jappsen A. K., Ballesteros-Paredes J., González R. F., Klessen R. S., 2007, *ApJ*, 657, 870
- Vázquez-Semadeni E., Palau A., Ballesteros-Paredes J., Gómez G. C., Zamora-Avilés M., 2019, *MNRAS*, 490, 3061
- Veena V. S., Vig S., Mookerjee B., Sánchez-Monge Á., Tej A., Ishwara-Chandra C. H., 2018, *ApJ*, 852, 93
- Vishniac E. T., 1994, *ApJ*, 428, 186
- Walder R., Folini D., 2000, *Ap&SS*, 274, 343
- Walsh C., Nomura H., Millar T. J., Aikawa Y., 2012, *ApJ*, 747, 114
- Walsh C., Millar T. J., Nomura H., Herbst E., Widicus Weaver S., Aikawa Y., Laas J. C., Vasyunin A. I., 2014, *A&A*, 563, A33
- Wang K., Testi L., Ginsburg A., Walmsley C. M., Molinari S., Schisano E., 2015, *MNRAS*, 450, 4043
- Xiong F., Chen X., Yang J., Fang M., Zhang S., Zhang M., Du X., Long W., 2017, *ApJ*, 838, 49
- Yuan J., et al., 2018, *ApJ*, 852, 12
- Zamora-Avilés M., Ballesteros-Paredes J., Hartmann L. W., 2017, *MNRAS*, 472, 647
- Zhang G.-Y., André P., Men'shchikov A., Wang K., 2020, *A&A*, 642, A76
- Zhou J.-W., et al., 2021, *MNRAS*, 508, 4639
- Zhu F.-Y., Wang J.-Z., Liu T., Kim K.-T., Zhu Q.-F., Li F., 2020, *MNRAS*, 499, 6018
- van Dishoeck E. F., Herbst E., Neufeld D. A., 2013, *Chemical Reviews*, 113, 9043

This paper has been typeset from a $\text{\TeX}/\text{\LaTeX}$ file prepared by the author.